AIAA SciTech Forum
8–12 January 2018, Kissimmee, Florida
2018 AIAA Aerospace Sciences Meeting

10.2514/6.2018-0543

Aerodynamic Analysis of NASA Common Research Model by Block-Structured Cartesian Mesh

Shinya Makino[1], Takaya Kojima[2], Takashi Misaka[3], Shigeru Obayashi[4]
Tohoku University, Sendai, Miyagi, Japan

Daisuke Sasaki[5]
Kanazawa Institute of Technology, Hakusan, Ishikawa, Japan

In this study, the aerodynamic analysis of NASA Common Research Model (wing-body configuration) was conducted by a block-structured Cartesian mesh method named Building-Cube method. The building-cube method (BCM) has the advantages of the quick and robust mesh generation and efficient parallel computing, and it is easy to run on a large-scale computing system. However, the BCM suffers a restriction on the resolution of the turbulent boundary layer. The aim of this study is to improve the resolution issue of the turbulent boundary layer at high Reynolds number flows using the immersed boundary method. By utilizing the advantages of the BCM, we challenge to resolve the boundary layer by mesh subdivision. In this paper, the results of the validation before subdivision mesh were shown by using a coarse mesh. The computational results were compared with the transonic wind tunnel test and the results of another flow solver. Although the results showed a similar tendency with the results of another flow solver, the decomposed aerodynamic coefficient appeared with some discrepancy.

Nomenclature

S_{ref}	=	Reference area
C_{ref}	=	Reference chord length
b_{ref}	=	Reference span length
C_L	=	Total lift coefficient
C_{Lp}	=	Pressure lift coefficient
C_{Lf}	=	Friction lift coefficient
C_D	=	Total drag coefficient
C_{Dp}	=	Pressure drag coefficient
C_{Df}	=	Friction drag coefficient
C_M	=	Pitching moment coefficient
C_P	=	Pressure coefficient
M	=	Mach number
Re	=	Reynolds number
T	=	Temperature
α	=	Angle of attack
x	=	Body axis coodinate in chord direction
y	=	Body axis coodinate in span direction
z	=	Body axis coodinate in vertical direction
η	=	Relative position of semi-span direction of the wing

[1] Graduate student, Institute of Fluid Science, 2-1-1 Katahira, Aoba-ku, Student Member AIAA.
[2] Graduate student, Institute of Fluid Science, 2-1-1 Katahira, Aoba-ku, Student Member AIAA.
[3] Assistant Professor, Institute of Fluid Science, 2-1-1 Katahira, Aoba-ku, Senior Member AIAA.
[4] Professor, Institute of Fluid Science, 2-1-1 Katahira, Aoba-ku, Associate Fellow AIAA.
[5] Associate Professor, Kanazawa Institute of Technology, 3-1 Yatsukaho, Hakusan, Senior Member AIAA.

I. Introduction

ALONG with the development of computers, computation fluid dynamics (CFD) simulation is used for aerodynamic design and development in various fields. Especially in the aircraft industry, it is utilized for estimating the performance with the help of CFD and wind tunnels. In the wind tunnel test, wind tunnel walls and model struts affect aerodynamic data, and there is a scale effect due to the different Reynolds number. It takes a huge cost to simulate the Reynolds number of the real scale model. Therefore, the accuracy improvement of actual aircraft performance estimation by a combination of wind tunnels and CFD is very important in the development of the aircraft industry.

In the current aircraft design by CFD, when we analyze a three-dimensional complex shape, an unstructured mesh is often adopted because mesh generation is easy for complex shape. However, the unstructured mesh has several issues in terms of calculation cost and computational accuracy. Therefore, it is difficult to make high order accuracy of spatial scheme and post-processing of big data calculation is high for the cost of processing[1,2]. Recently, Cartesian mesh method is drawing an attention as a method to solve these problems. Building-cube method (BCM) which is a type of Cartesian mesh method was proposed by Nakahashi as the data structure that can easily realize parallel calculation indispensable for large-scale calculation[3]. BCM can be expected for analysis of complicated flow fields such as wake flow and vortex because it can easily make higher order accuracy of space by using an equally Cartesian mesh. On the other hand, when expressing a curved surface using a Cartesian mesh, the surface of the object is expressed stepwisely. Therefore, it is necessary to improve the calculation precision near the object. In order to improve the calculation accuracy, it is expected to reduce the influence of stepwise expression and it is necessary to increase a lot of grid points. Especially, a practical problem in the aeronautics field is high Reynolds number flow, and the above-mentioned problem concerning the resolution of the boundary layer becomes a problem[3-5].

To utilize the advantage of the Cartesian mesh method, measures to apply special processing near the object surface are adopted. This method can solve the above problems, and many researches are being conducted. In the research of Ishida et al., they are trying to improve the calculation precision near the object by using the hybrid approach of Immersed Boundary Method (IBM) and gridless method[6]. Haga et al., they are dealing with the hybrid unstructured mesh of Cartesian and object-adaptive mesh[7]. Tamaki et al., they use countermeasures by giving the correct velocity distribution near the object surface by using wall models[8]. Various approaches near the object surface are studied like these. Our research group is studying two approaches near the object surface. The first approach is overset method with the unstructured mesh. We investigate how to improve the boundary layer resolution by using unstructured mesh near the object surface. The unstructured mesh method is a computation method that is suitable for complex shapes because the unstructured mesh has high mesh arrangement flexibility. Therefore, it is a calculation method suitable for complex shapes like an actual shape of aircraft. Furthermore, the Cartesian mesh can be analyzed efficiently near the object by overlapping with other grid methods. In addition, it is possible to analyze wake flows and vortices in detail by the Cartesian uniformity in the far field and spatial analysis accuracy. The second approach is Cartesian mesh method using IBM. IBM is a technique to simulate the original object shape by wall boundary conditions. It can calculate the model without changing the grid shape of the Cartesian mesh on the wall surface. Therefore, IBM is expected because it can be used without losing the ease of mesh generation and the robustness. Recently, in the case of calculation using Cartesian mesh method, IBM and wall model are well adopted near the object surface[9]. However, it is necessary to do special processing in the non-linear problem contrary to wall law, and the process becomes complicated. Therefore, we investigate how to improve the boundary layer resolution using mesh subdivision by BCM which is good at large scale calculation.

In the previous study, it was confirmed that the results of the BCM and near-wall unstructured overset mesh were generally agreed well with the experiment in aerodynamic predictions[10]. However, the benefits of Cartesian mesh cannot be fully explored in this method, especially, in term of mesh generation and calculation cost. Therefore, it is desired to calculate only with the Cartesian mesh in order to fully utilize the Cartesian mesh approach.

The aim of this study is to improve the Cartesian mesh resolution of the turbulent boundary layer at high Reynolds number flows using BCM with IBM. In this study, we calculate the flow around NASA Common Research Model by using the BCM solver with IBM, and the results are compared with the experiment and the result of BCM-TAS coupling solver. Throughout this study, the effectiveness of BCM for the calculation of flow around the aircraft at high Reynolds number is also discussed.

II. Numerical Method

A. Building-Cube Method (BCM)

Building-cube method (BCM) is based on the multi block-structured of equally-spaced Cartesian mesh. The equally-spaced Cartesian mesh has the merit of the simplicities in the mesh generation, in the spatially higher-order solution algorithm, and in the post-processing. To adapt the mesh resolution to the local flow scale without introducing the algorithm complexity, a block-structured Cartesian mesh approach was employed in the BCM[3,4]. The characteristic of the BCM is that there is no bias in the calculation load at parallel calculation and it is good at parallelization efficiency. This characteristic is obtained by the calculation for each divided calculation area using equally-spaced Cartesian mesh.

The way of BCM calculation is dividing the entire computational domain into small square domain named 'Cube'. The size of all Cube differs by a multiple of 2^n. Subsequently, the same number of the computational mesh is generated in each Cube, named 'Cell'. Cubes and Cells in the BCM are arranged as shown in Fig. 1. There are two types of Cells, Fluid Cell and Wall Cell. Cells in the fluid region are defined as Fluid Cell, and the cells at wall boundary or inside wall region are defined as Wall Cell. Individual Cubes are computed independently, thus the BCM needs to exchange physical quantity between the adjacent Cubes during the computational process. In order to exchange physical quantity, all Cubes have additional three layers of Cells at each side, named Overlap Cell, as shown in the shaded area of Fig.2. Overlap Cell is arranged to overlap adjacent Cube. Therefore, at the exchange process, Cubes of the same size can maintain the interpolation accuracy at Cube boundaries. However, in the case of Cubes of different size between adjacent Cubes, linear interpolation is conducted as shown in Fig. 3. In the case of exchanging information from a small Cell to a large Cell, the physical quantity is given by the first-order interpolation as shown in Fig. 3(a). In the case of exchanging information from a large Cell to a small Cell, the physical quantity is given by zero-order interpolation as shown in Fig. 3(b).

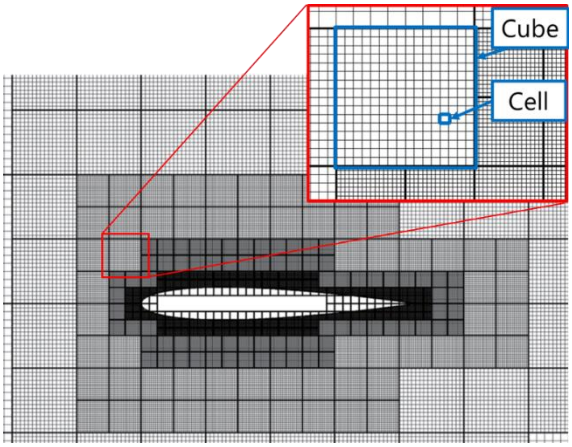

Figure 1. Composition of Cubes and Cells in BCM

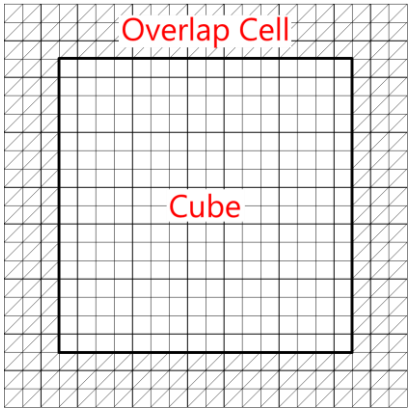

Figure 2. Cells and Overlap Cells in each Cube

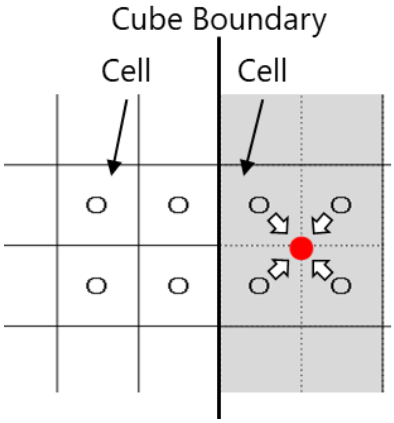

(a) Exchange information from small to large

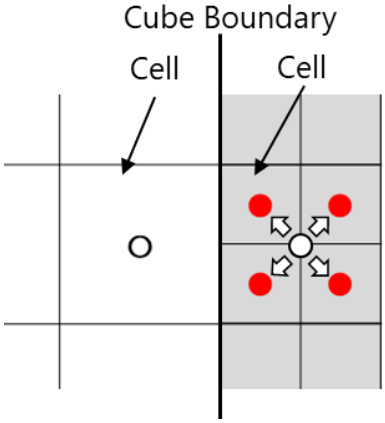

(b) Exchange information from large to small

Figure 3. Handling of physical quantities at Cube boundary

B. Numerical method for the compressible Navier-Stokes equations

The governing equation is three-dimensional compressible Navier-Stokes equations. A non-dimensional form of the three-dimensional compressible Navier-Stokes equations can be written in the form as,

$$\frac{\partial}{\partial t}\boldsymbol{Q} + \frac{\partial}{\partial x_j}\boldsymbol{F}_j - \frac{1}{Re}\frac{\partial}{\partial x_j}\boldsymbol{G}_j = 0 \tag{1}$$

Where $\boldsymbol{Q} = [\rho, \rho u, \rho v, \rho w, e]^T$ is the vector of conservative variables, ρ is the density, u, v, w are the velocity components in the x, y, z directions and e is the total energy. Re is the Reynolds number. $\boldsymbol{F}_j$ and $\boldsymbol{Gj}$ are inviscid and viscous flux tensor.

The discretization method is a cell-centered finite volume method. The viscous calculations is calculated by using Spalart-Allmaras turbulence model. The viscous flux is computed using second-order central difference method. The numerical flux is computed using a Simple Low-dissipation AUSM (SLAU) scheme. Time integration method is a Lower-Upper Symmetric Gauss-Seidel (LU-SGS) implicit time integration method[11-13].

C. Wall boundary conditions

In this study, the wall boundary condition was given value by Immersed Boundary Method (IBM). The adopted IBM is based on Ghost-cell approach, and it provides appropriate physical value to Ghost-cells to set a viscous wall boundary condition (non-slip) according to the location of an object surface. This method was referred to the method proposed by Mittal et al[14]. Ghost-cell is defined as the cell locates inside the solid region surrounded with at least one fluid cell. Image Points are set at normal direction of Ghost-cells according to the geometry data of CAD. A distance between Image Points to Ghost-cells is fixed to 1.75 times of minimum mesh spacing. Subsequently, physical value of Image Points is interpolated from the adjacent 27 cells of Image Points using distance dependent weighting. The physical value of Ghost-cells is decided from that of Image Points according to a distance from the 27 cells to Image Points. The boundary conditions for viscous flow computations are given by the following equations. The velocity magnitude at a Ghost-cell is evaluated according to the distance for setting a velocity to zero on an object. Static pressure and density are evaluated by zero-order interpolation.

$$\boldsymbol{u}_{GC} = -\frac{d_{GC}}{d_{IP}} \times u_{IP} \tag{2}$$

$$p_{GC} = p_{IP} \tag{3}$$

$$\rho_{GC} = \rho_{IP} \tag{4}$$

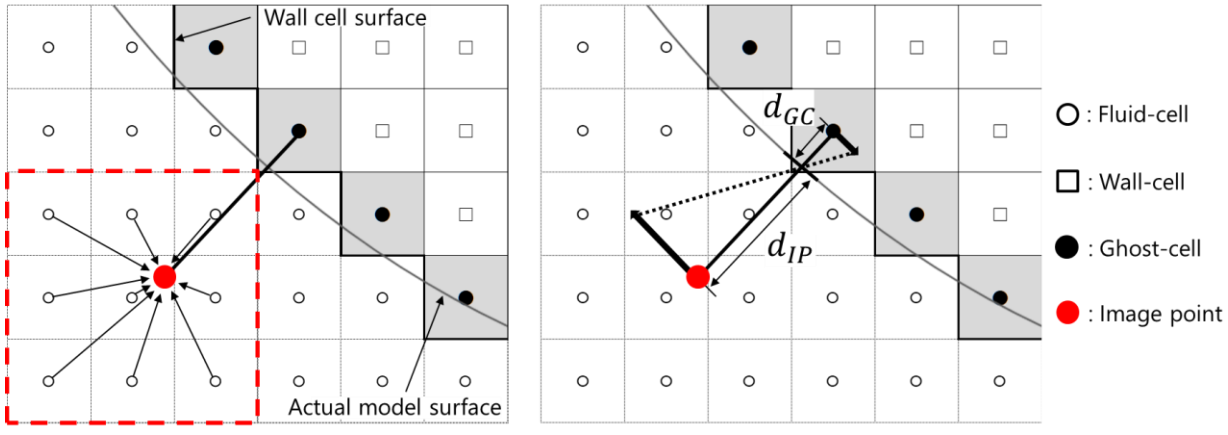

(a) Calculate physical quantity at Image Point (b) Calculate velocity at Ghost-cell

Figure 4. Handling of Ghost-cell at wall boundary

D. Overall computational procedure

A flow chart of the present computation is given in Fig. 5. First, the wall boundary condition is defined by the BCM mesh and geometry data after initial setting which includes determination of Ghost-cells, definition of corresponding image points, calculation of the wall distance, and so on. Then, the flow computation for Navier-Stokes equation is performed for each Cube using initial condition and wall boundary condition. These processes are parallelized by OpenMP. After that, the mesh is subdivided in this study. The mesh is subdivided from the result of the converged coarse mesh. At that time, the physical quantity and the wall distance are given by interpolation from coarse mesh information, and tri-linear interpolation is adopted. The interpolation is produced to cell-center of the subdivided mesh from cell-center values of the coarse mesh of 8 points in the vicinity. This procedure can reduce the pre-processing time and the calculation time.

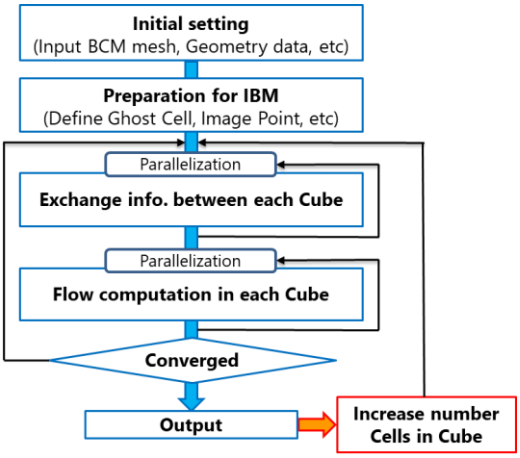

Figure 5. Flow chart

III. Computational Conditions

A. Flow Condition

The computational condition is decided by reference to Aerodynamics Prediction Challenge (APC). APC was a workshop held by Japan Aerospace Exploration Agency (JAXA), and was held in order to improve the prediction accuracy of aerodynamic performance of an aircraft[15]. The conditions of aerodynamics prediction analysis is shown in Table 1. These conditions are set considering the cruising state. In the condition of aerodynamics prediction analysis, Mach number is 0.847, angle of attack is set in nine cases from -1.79 [deg] to 5.72 [deg]. However, the calculation is done with only four Angles of attack (-0.62, 2.94, 4.65, 5.72 [deg]) in this study. Reynolds number is 2.26×10^6, the temperature is 284 [K].

Table 1. Analysis conditions

Mach number	0.847
Reynolds number	2.26×10^6
Temperature [K]	284.0
Angle of Attack [deg]	-1.79, -0.62, 0.32, 1.39, 2.47, 2.94, 3.55, 4.65, 5.72

B. Model for Analysis

We calculated a flow around the NASA Common Research Model (CRM), which is shown in Fig. 6. The CRM is an aircraft model developed by NASA and Boeing, which is based on a civil aircraft cruising at transonic speed in the AIAA Drag Prediction Workshop[16]. Table 2 shows the model scale of CRM by using JAXA wind tunnel test. In this study, we calculated models by using the half-cutting model of CRM. The aerodynamic deformation of the main wing is considered at each angle of attack according to the experimental data, and it was considered by geometry data of CAD[17].

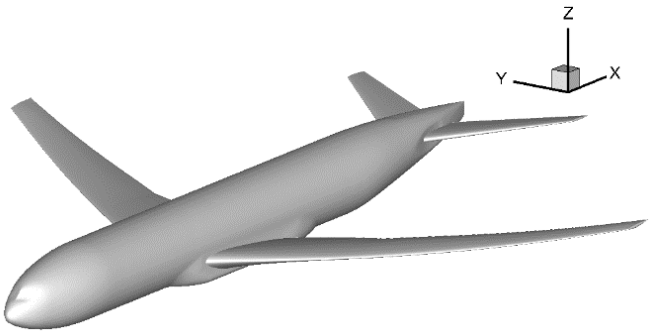

Figure 6. NASA Common Research Model (CRM)

Table 2. Model scale of CRM

Reference area S_{ref} [m^2]	0.179014
Reference chord length C_{ref} [m]	0.15131
Reference span length b_{ref} [m]	1.2692
Moment center position (x, y, z) [m]	(0.72741, 0.0 0.09762)

C. Computational Mesh

The BCM mesh was calculated separately for some levels of fineness. However, only the result of the Coarse mesh is listed in this paper. Table 3 is a mesh information before subdividing mesh, and it is shown information for validation by the Coarse mesh. The subdividing mesh is made by changing the number of the Cells inside the Cube. Therefore, the number of the Cube in all mesh is the same. The number of the Cells on the one side of Cube is set to increase as a mesh get finer. In the subdividing mesh, the calculation is started by interpolating the physical quantity in each Cube from the result of the Coarse mesh. Figure 7 shows the overview of the Cube near the wall surface. Figure 8 shows the Cube in the wing section, and Fig. 9 shows the BCM mesh on the wing top. The pressure coefficients shown in the next chapter are obtained from the acquisition section in Fig. 10.

Table 3. Mesh Information

Angle of Attack [deg]	-0.62	2.94	4.65	5.72
Number of Cubes	362,527	362,527	362,527	362,527
Number of Cells	1,484,910,592	1,491,992,576	1,493,143,552	1,495,793,664
Min. Cell size	0.0001526	0.0001526	0.0001526	0.0001526
Number of Cells in a Cube	16×16×16	16×16×16	16×16×16	16×16×16

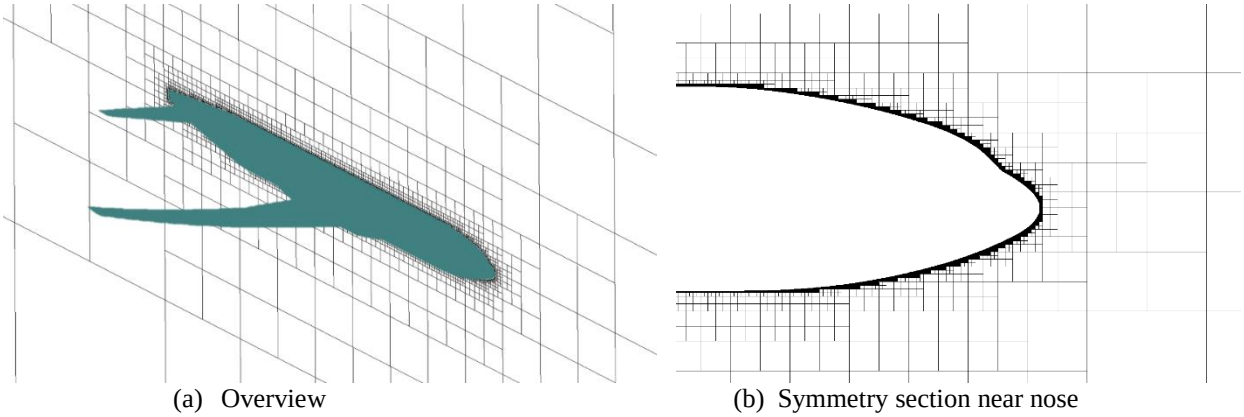

(a) Overview (b) Symmetry section near nose

Figure 7. Arrangement of Cubes near the wall surface

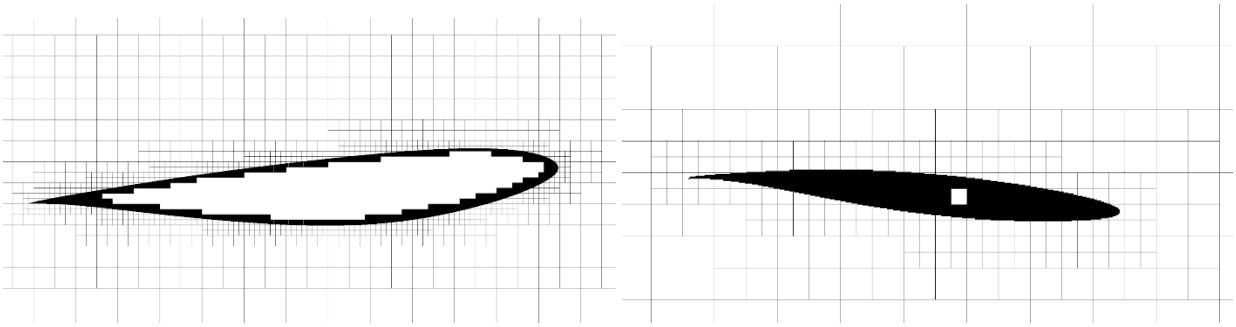

(a) Wing root ($\eta = 0.131$) (b) Wing tip ($\eta = 0.950$)

Figure 8. Arrangement of Cubes on wing section

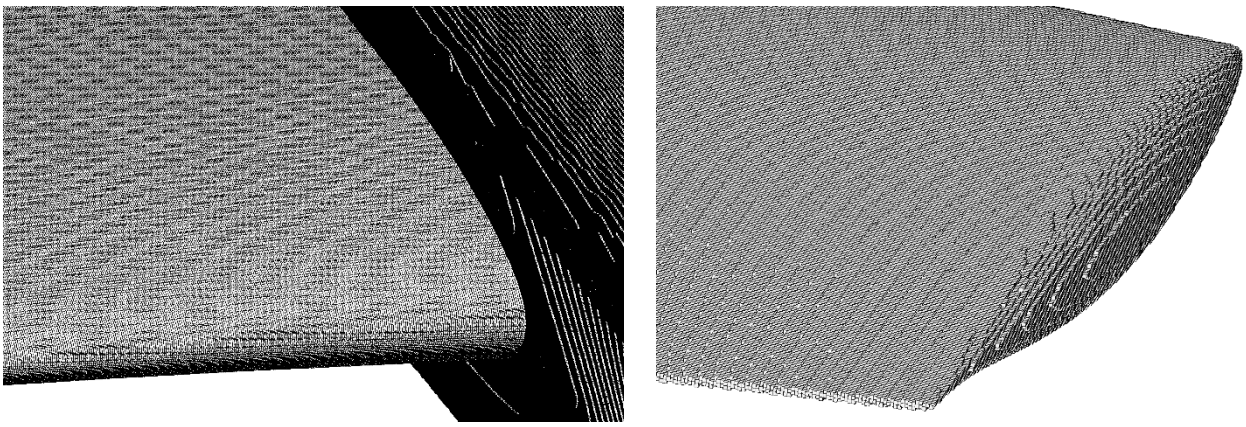

(a) Wing root ($\eta = 0.131$) (b) Wing tip ($\eta = 0.950$)

Figure 9. BCM mesh on wing top

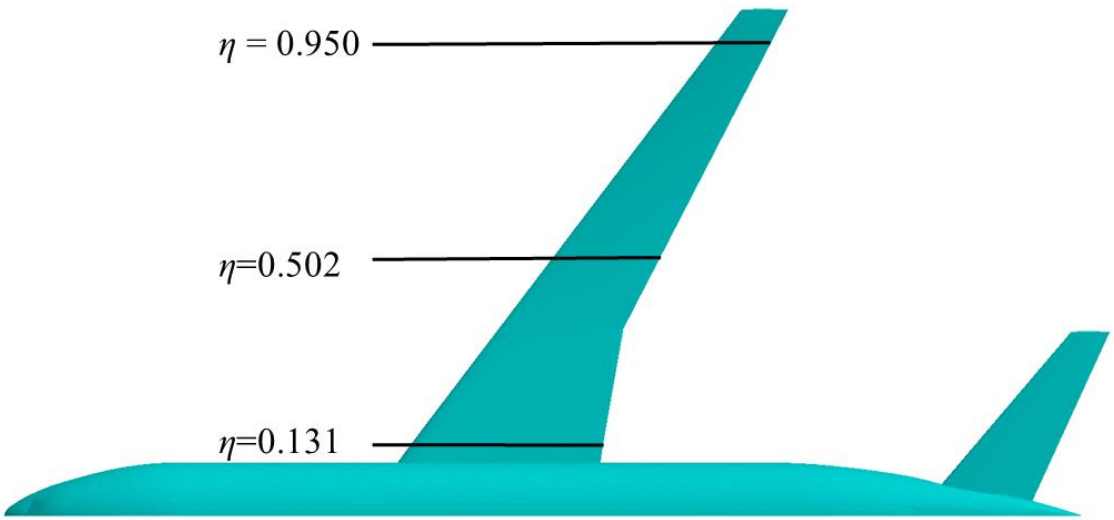

Figure 10. Definition of the wing sections

IV. Computational Results

A. Aerodynamics Coefficient

Each aerodynamic coefficients C_L and C_D versus the angle of attack are shown in Figs. 11 and 12, respectively. The result of TAS shown in Fig. 11 corresponds to the calculation result with an unstructured mesh solver[18]. Figure 13 shows the decomposed result of each aerodynamic coefficient. The lift coefficient C_L of the BCM shows a similar tendency with the result of the BCM-TAS coupling solver at each angle of attack, but the C_L appears smaller then the BCM-TAS result. Figure 13(a) shows a discrepancy with the same levels at all angles of attack. Although Fig. 13(c) also has a discrepancy, there is no large influence on the prediction accuracy of C_L. Therefore, it is confirmed that the discrepancy of C_{Lp} significantly affected the prediction accuracy of C_L. The drag coefficients C_D was predicted larger at -0.62 [deg]. At the other angle of attack (2.94, 4.65, 5.72 [deg]), the C_D shows a similar tendency with the result of the BCM-TAS coupling solver. However, this agreement is not reliable because the pressure drag coefficient and friction drag coefficient don't match the result of the BCM-TAS coupling solver as illustrated in Figs. 13(b) and (d). These discrepancies are also the same levels at all angle of attack. We will validate how much improvement of the discrepancy will be made by the subdivision mesh in the near future. One of the reasons why the experimental value differs from the result of the BCM-TAS coupling solver is the effect of struts.

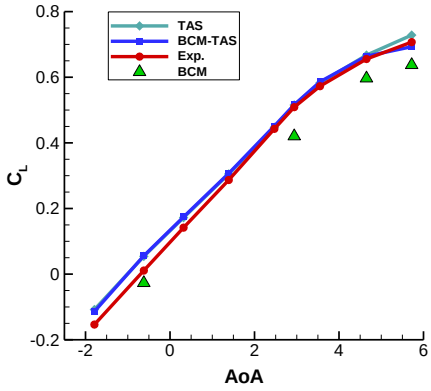

Figure 11. Lift coefficient distribution

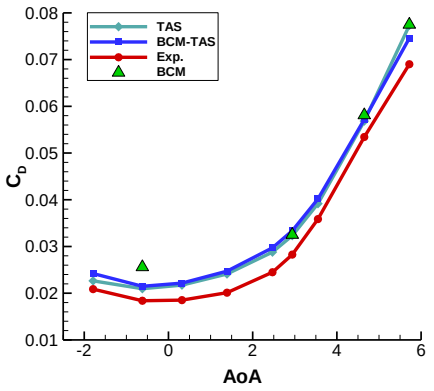

Figure 12. Drag coefficient distribution

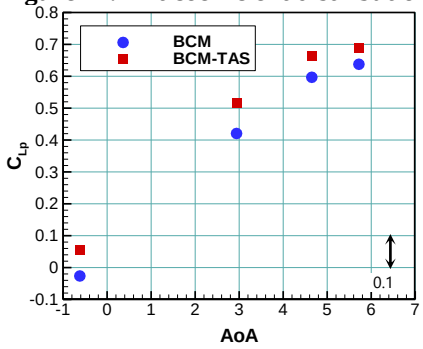

(a) $C_{Lp} - \alpha$

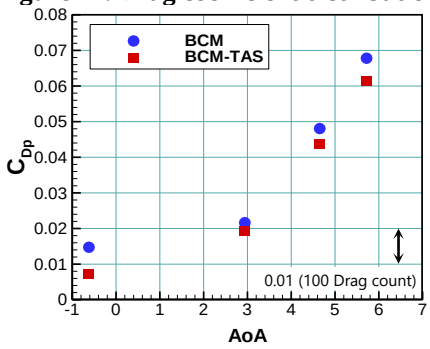

(b) $C_{Dp} - \alpha$

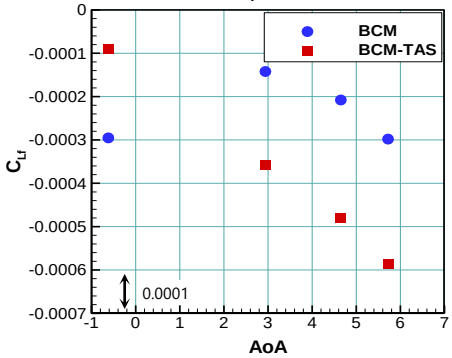

(b) $C_{Lf} - \alpha$

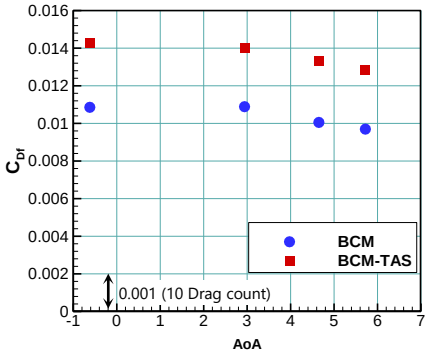

(d) $C_{Df} - \alpha$

Figure 13. Decomposition aerodynamics coefficient

B. Pressure Coefficient of Wing Surface

Each pressure coefficient of wing surface corresponding to the angle of attack (-0.62, 2.94, 4.65, 5.72 [deg]) is shown in Figs. 14 to 17. These pressure coefficients are acquired in the cross-section of the wing shown in Fig. 10 (η=0.131, 0.502, 0.950). At the Angle of attack α =-0.62 [deg], the pressure coefficient shows similar values to the results of BCM-TAS coupling solver for the wing root side (η =0.131). It also shows similar values to the experimental results. However, the pressure coefficient on the bottom side is different compared with the results of BCM-TAS coupling solver for the wing tip side. Furthermore, the pressure coefficient of trailing edge is not well-predicted. It is considered that the pressure coefficient of trailing edge was affected by the shape reproduction precision. At the angle of attack α =2.94 [deg], the pressure coefficient differs in the shockwave generated position for the wing root. Thus, it can be seen that the separation was not captured in the wing root (η=0.131). In the intermediate section (η=0.502), the shockwave of BCM has predicted a position ahead of the experimental results and the results of BCM-TAS coupling solver. Fig. 18 shows the pressure coefficient contour at the angle of attack α =2.94 [deg]. In Fig. 18, the negative pressure region is predicted slightly forward compared to the BCM-TAS coupling solver. Furthermore, the negative pressure at the leading edge is predicted large value in the BCM. At the Angle of attack α =4.65 [deg], the pressure coefficient differs in the shockwave generated position for the wing root as with angle of attack α =2.94 [deg]. In the intermediate section (η=0.502), the results of the BCM did not predict a shockwave accurately. The suction peak is not captured at the wing tip (η =0.950), and the pressure coefficient distribution does not match with the results of BCM-TAS coupling solver. Fig. 19 shows the pressure coefficient contour at the angle of attack α =4.65 [deg]. In Fig. 19, the negative pressure region is predicted slightly forward compared to the BCM-TAS coupling solver. The negative pressure at the leading edge was predicted large value as shown in Fig. 19. At the angle of attack α =5.72 [deg], the pressure coefficients show a similar tendency with the results of BCM-TAS coupling solver, however it differs in the shockwave generated position for the wing root as with angle of attack α =4.65 [deg]. The pressure coefficient distribution does not match with the results BCM-TAS coupling solver at other section.

From these results, it was confirmed that the negative pressure was predicted to be large at the leading edge compared with the results of BCM-TAS coupling solver. The results showed that the separation region shifted forward on the whole. The separation at wing root was not accurately captured at α = 2.94, 4.65, 5.72 [deg]. In the results of the current coarse mesh, it was confirmed that the shape of the wing tip and trailing edge are not accurately reproduced.

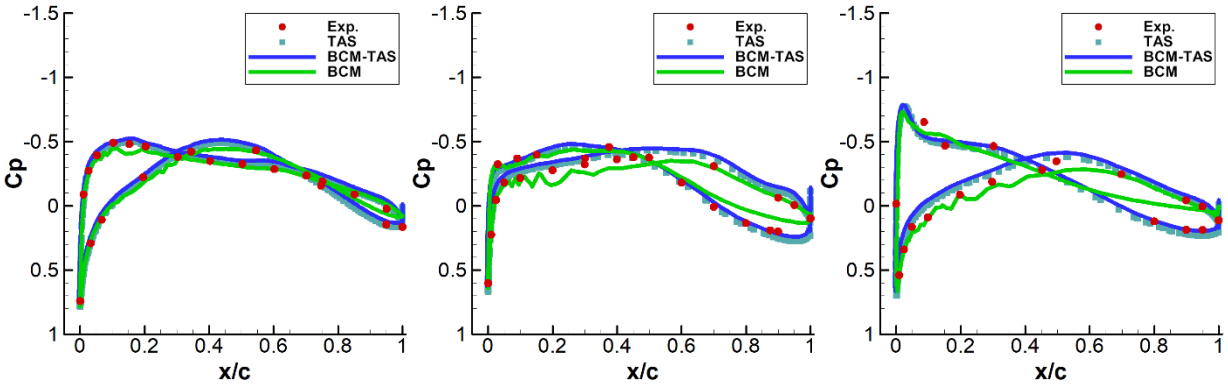

(a) η=0.131 section (b) η=0.502 section (c) η=0.950 section

Figure 14. Pressure coefficient at α =-0.62[deg]

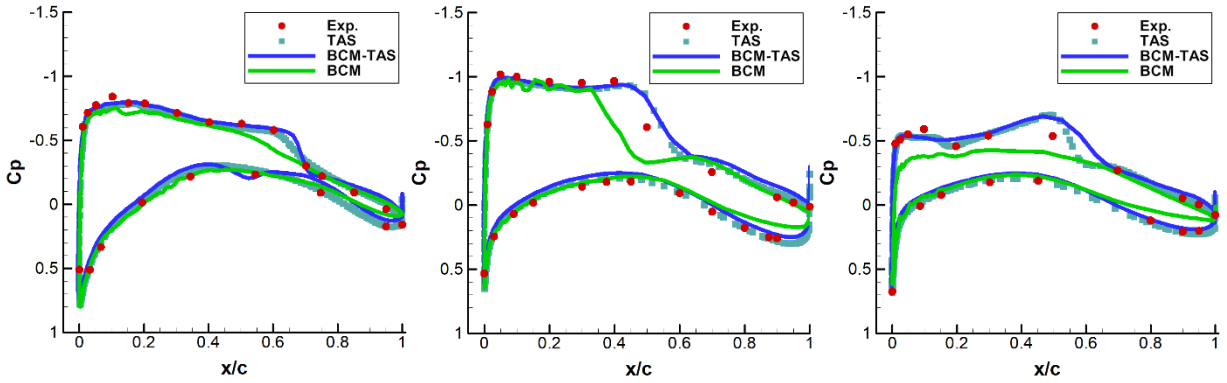

(a) η=0.131 section (b) η=0.502 section (c) η=0.950 section

Figure 15. Pressure coefficient at α =2.94[deg]

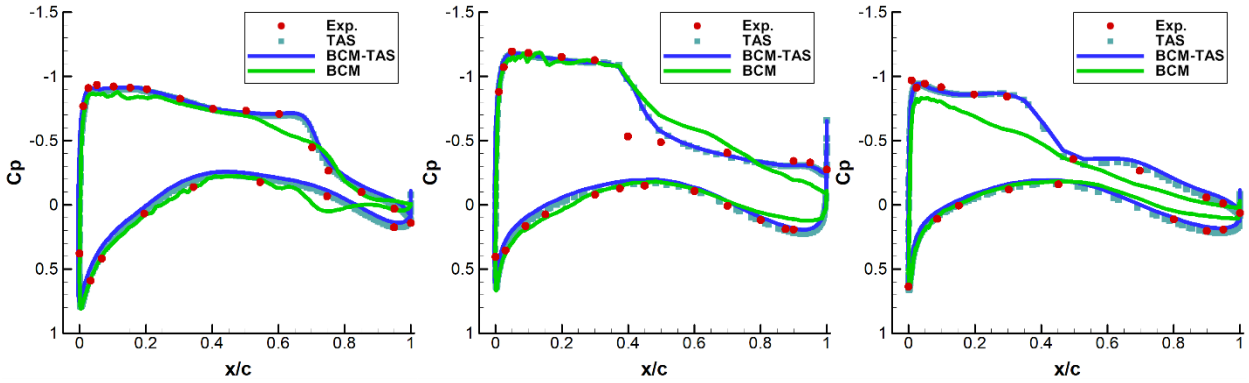

(a) η=0.131 section (b) η=0.502 section (c) η=0.950 section

Figure 16. Pressure coefficient at α =4.65[deg]

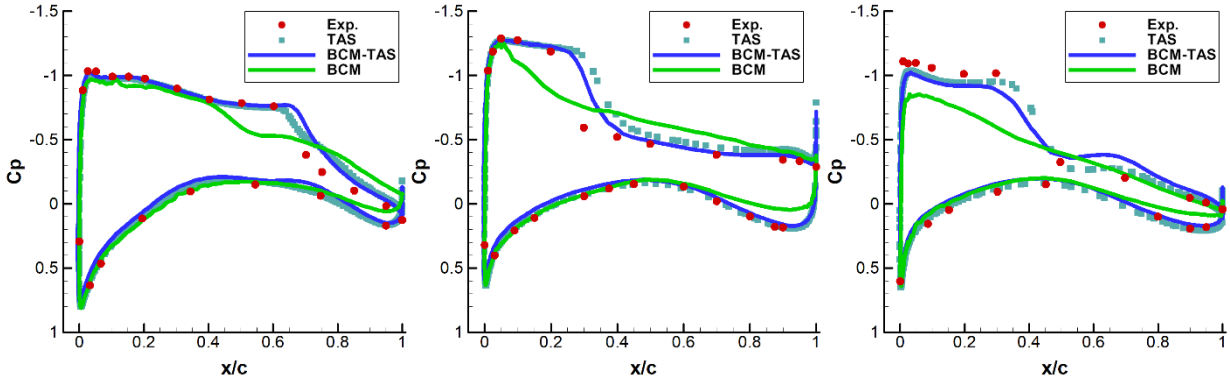

(a) η=0.131 section (b) η=0.502 section (c) η=0.950 section

Figure 17. Pressure coefficient at α =5.72 [deg]

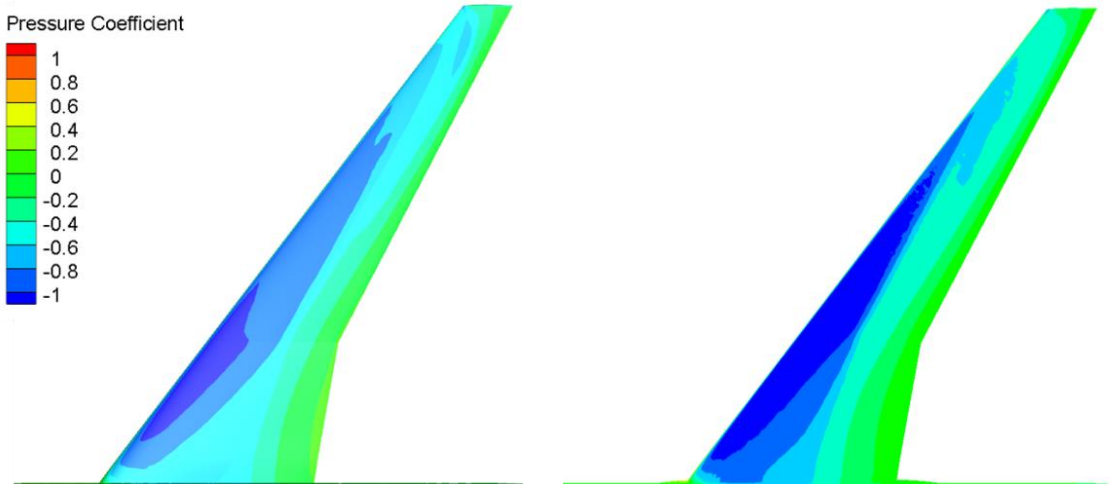

(a) BCM-TAS Coupling (b) BCM

Figure 18. Contour of pressure coefficient at 2.94 [deg]

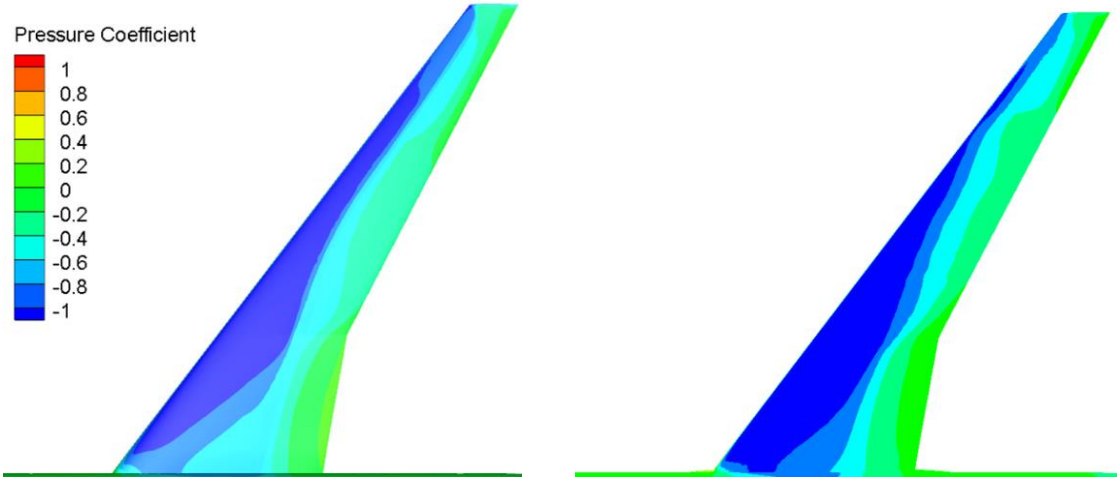

(a) BCM-TAS Coupling (b) BCM

Figure 19. Contour of pressure coefficient at 4.65 [deg]

V. Conclusion

In this study, the aerodynamics prediction was performed by using the BCM solver with IBM, and the results were compared with the experiment and the results of the BCM-TAS coupling solver. In this paper, the results of the validation before subdivision mesh were shown by using a coarse mesh. Although the lift coefficient showed a similar tendency, it was predicted the small values compared with the experiment and the results of the BCM-TAS coupling solver. We confirmed that the pressure component was estimated to be too small by the decomposition of the aerodynamic coefficient. In the drag coefficient, the friction drag was predicted smaller, and the pressure drag was predicted larger than that of another solver. In the pressure coefficient, the negative pressure was predicted to be large at the leading edge compared with the results of BCM-TAS coupling solver, and the results showed that the separation region shifted forward along the span. Furthermore, we confirmed that the separation was not captured near the wing root.

In the near future, we will consider improving the prediction accuracy of the BCM using subdivision mesh. We will investigate the problem in detail such as the increase of negative pressure on the leading edge, the prediction accuracy of separation on the wing root, and so on.

Acknowledgments

The computational results in this research were obtained using supercomputing resources at Advanced Fluid Information Research Center of the Institute of Fluid Science, Tohoku University.

References

[1]Ito, Y. and Nakahashi, K., "Direct Surface Triangulation Using Stereolithography Data," AIAA Journal, Vol. 40, No. 3, pp. 490-496, 2002.

[2]Ito, Y. and Nakahashi, K., "Surface Triangulation for Polygonal Models Based on CAD Data," International Journal for Numerical Methods in Fluids, Vol. 39, pp. 75-96, 2002.

[3]Nakahashi, K. and Kim, L. S., "Building-Cube Method for Large-Scale, High Resolution Flow Computations," AIAA Aerospace Sciences Meeting and Exhibit, 2004-434.

[4]Nakahashi, K., "Immersed Boundary Method for Compressible Euler Equations in the Building-Cube Method," 20st AIAA Computational Fluid Dynamics Conference, 2011-3386.

[5]Hashiba, M., Sasaki, D. and Nakahashi, K., "Development of Cartesian-Mesh Based CFD Solver Combined with Unstructured-Mesh,",8th International Conference on Flow Dynamics, 2011.

[6]Ishida, T. and Nakahashi, K., "Immersed Boundary Method for Compressible Turbulent Flow Computations in Building-Cube Method," 21st AIAA Computational Fluid Dynamics Conference, 2013-2451.

[7]Haga, T., Kuzuu, K., Takaki, R. and Shima, E., "Development of a High-Order Flux Reconstruction Scheme for Body-Fitted Cartesian Unstructured Grids," 51st AIAA Aerospace Sciences Meeting Including the New Horizons Forum and Aerospace Exposition, 2013-409.

[8]Tamaki, Y., Harada, M., Imamura, T., "Near-Wall Modification of Spalart-Allmaras Turbulence Model for Immersed Boundary Method," AIAA Journal, Vol.55, No.9, 2017.

[9]Capizzano, F., "Coupling a Wall Diffusion Model with an Immersed Boundary Technique," AIAA Journal, Vol. 54, No.2, pp. 728-734, 2016

[10]Makino, S., Misaka, T., Obayashi, S., Hirose, T., Sasaki, D., "Aerodynamics Analysis of NASA Common Research Model Using BCM-TAS Coupling Flow Solver," JSASS Jounal, 2017, accepted (in Japanese).

[11]Spalart, P. R., Allmaras, S. R., "A One-Equation Turbulence Model for Aerodynamic Flows," AIAA Paper 1002-0439, 30th Aerospace Sciences Meeting and Exhibit, 1992.

[12]Shima, E. and Kitamura, K., "Parameter-Free Simple Low-Dissipation AUSM-Family Scheme for All Sppeds," AIAA Journal, Vol.49, No.8, pp. 1693-1709, 2011.

[13]Yoon, S. and Jameson, A., "Lower-upper Symmetric-Gauss-Seidel method for the Euler and Navier-Stokes equations," AIAA Journal, Vol. 33, No. 6, pp. 1134-1141, 1995.

[14]Mittal, R., Dong, H., Bozlurttas, M., Najjar, F. M., Vargas, A., Von Loebbecke, A., "A versatile sharp interface immersed boundary method for incompressible flows with complex boundaries," Journal of Computational Physics, Vol. 227, pp.4825-4852, 2008.

[15]https://cfdws.chofu.jaxa.jp/apc/ [retrieved on December 4th, 2017]

[16]https://aiaa-dpw.larc.nasa.gov/ [retrieved on December 4, 2017]

[17]Ueno, M., Kohozai, M. and Koga, S., "Transonic Wind Tunnel Test of the NASA CRM: Volume 1," JAXA Research and Development Memorandum, JAXA-RM-13-017E, 2014.

[18]Nakahashi, K., Ito, Y. and Togashi, F., "Some challenges of realistic flow simulations by unstructured grid CFD," International Journal for Numerical Methods in Fluids, Vol. 43, pp.769-783, 2003.